Chapter 3
Fabrication of Conducting Perovskite Oxide Nanowires

3-1 Introduction

This work is based on earlier detailed studies of growth dynamics of oxide thin films. It has been shown that different growth modes, such as island growth, layer-by-layer growth, and step-flow growth can be chosen at will by selecting suitable growth parameters[i]. Careful growth mode control has been used for growing a variety of oxide nanostructures[ii] such as dots, wires, and rings. There are several methods that can be used to characterize the dimensions of nanostructures. For example, scanning probe techniques, optical characterization[iii], and electrical measurements can be used. Scanning probe techniques can only access the sample surface, which means that only nanostructures that are exposed can be directly imaged. From the point of view of electrical characterization, however, this presents a problem, because various dead layers[iv,v,vi], surface or interface states[vii], and charge transfer layers[viii] are formed in many practical oxide structures. The properties of exposed nanostructures are therefore dominated by surface effects and do not reflect the properties of the nanostructures if such structures are embedded in a crystal. While this problem can be solved by covering the nanostructures with capping layer, it also makes it impossible to image the nanodots or nanowires directly by scanning probes..

The aim of this work was to fabricate conducting nanowires composed of a perovskite oxide. Fabricating conducting nanowires is a good first step in obtaining nanowires that could be used for measuring transport and other properties of oxides in confined geometries.

One-dimensional structures are currently intensively studied as promising candidates for use in next generation electronic devices. Even the mainstream silicon device manufacturing has by now reached the 45 nm technology node and further size reductions are foreseen. This has prompted the development of various nanoscale devices, such as single electron transistors and organic molecular devices. At the same time, device interconnect technology has seen much less development. Except for use as molecular-level interconnects, nanowires are also interesting because one-dimensional metal or semiconductor structures can show quantum

conductance effects[ix]. A nanowire-channel transistor[x,xi] is expected to show high carrier mobility due to energy quantization in perpendicular direction to wires. Nanowires have also been proposed for use in gas sensor[xii,xiii,xiv] due to their high aspect ratios.

References

[i] M. Lippmaa et al., Appl. Phys. Lett., **76**, 2439 (2000)
[ii] M. Lippmaa et al., Proc. SPIE Int. Soc. Opt. Eng., **4467**, 128 (2001)
[iii] T. Kitahara et al., Appl. Surf. Sci. **219**,271 (2003)
[iv] J. Z. Sun et al., Appl. Phys. Lett., **74**, 3017 (1999)
[v] M. Ziese et al., J. Appl. Phys., **91**, 9930 (2002)
[vi] D. H. Kim et al., Solid State Commun., **114**, 473 (2000)
[vii] A. Ohtomo et al., Appl. Phys. Lett., **84**, 1716 (2004)
[viii] H. Yamada et al. Science, **305**, 646 (2004)
[ix] A. Kristensen et al., J. Appl. Phys., **83**, 607 (1998)
[x] X. Duan et al., Nature, **425**, 274 (2003)
[xi] S. J. Kim et al., Physica B, **272**, 117 (1999)
[xii] A. Kolmakov et al., Adv. Mater., **15**, 997 (2003)
[xiii] D. Zhang et al., Appl. Phys. Lett., **83**, 1845 (2003)
[xiv] X. Liu et al., Appl. Phys. Lett. **82**, 1950 (2003)

3-2 Fabrication method of nanowires

Step-flow growth was used to fabricate the nanowire films by depositing $LaTiO_x$ at very high temperature, where surface migration leads to the deposited material decorating the step edges of the substrate. Before film growth, the substrate surface can be viewed as an atomic landscape of terraces, separated by steps with a monolayer height. This is called a step-and-terrace surface. Microscopic processes in epitaxial growth include the deposition of atoms or molecules on the terraces of the substrate, adatom (adsorbed atom) desorption from the terraces, adatom diffusion on the terraces, and attachment or detachment of adatoms to and from the step edges. If adatom attachment at step edges dominates, the position of the step edge changes, inducing vertical growth of the film by 'step-flow'. The key to nanowire growth is the step-flow mechanism.

Step-flow growth can occur if the growth temperature is high enough for adatoms to migrate to step edges. The process can be observed in situ by monitoring the RHEED specular spot intensity. The characteristic step-flow RHEED intensity behavior is shown in Fig.3-2. After every excimer laser pulse, the RHEED intensity drops sharply due to a momentary increase of surface roughness. The intensity then gradually recovers as adatoms are attached to step edges. This recovery time is strongly temperature dependent and the laser pulse rate should be adjusted so as to give time for all surface adatoms to diffuse to the step edges before the next deposition pulse.

Nanowire films can be formed by depositing in step-flow mode a layer that covers less than a full monolayer. Most of the practical semiconductor devices that require epitaxial growth are fabricated by using step-flow growth because better performance due to higher crystal quality can be obtained than during layer-by-layer growth. This is true for oxides as well, for example, $SrTiO_3$ films grown by step-flow are known to show significantly better dielectric constants, exceeding 10^4, than films grown in layer-by-layer mode[i].

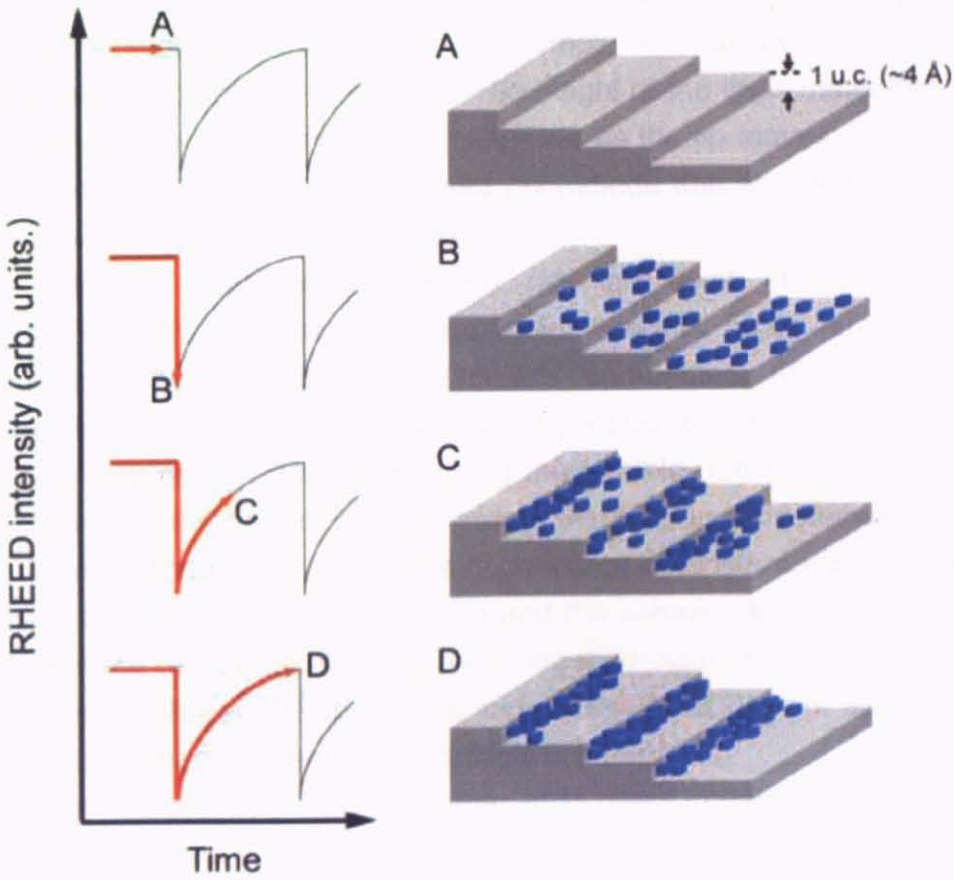

Fig.3-2 Schematic of step-flow growth and typical behavior of RHEED intensity

Reference

[i] M. Lippmaa et al., Appl. Phys. Lett., **74**, 3543 (1999)

3-2 Characterization system of wires

3-2-1 Atomic Force Microscopy

Atomic force microscope (AFM) is a scanning probe microscope that is used to measure the surface morphology of samples with a nanometer-scale accuracy. In this method, the surface height information is obtained by scanning a probe needle over the sample surface and measuring the needle position at each point on the surface. The basic building blocks of a typical AFM are shown in Fig.3-2-1. In a basic AFM setup, the sharp scan needle is attached to a flexible cantilever. A piezoelectric drive is used to scan either the tip or the sample so that the tip can be placed anywhere within a rectangular scan area. The height of the tip is measured optically, by detecting the deflection of the elastic cantilever as the tip moves up or down. The optical detection is done with a segmented photodiode that can detect both vertical and lateral movement of the reflected light beam.

Various different measurement modes can be used in commercial AFM instruments. Recently, several AFM equipment vendors have introduced a new imaging mode, a hybrid form of contact and non-contact AFM modes. In this so-called tapping mode[i], the cantilever (driven by a piezoelectric actuator) vibrates at its resonance frequency. Upon approaching the sample, the tip briefly touches, or taps, the surface at the bottom of each swing, resulting in a decrease in oscillation amplitude. The feedback loop keeps this decrease at a constant value by increasing or decreasing the distance between the tip and the sample. A topographic image of the sample surface can be obtained by recording the height information at each point. The contact force between the tip and the surface can be 200 pN or less, making this measuring mode especially useful for relatively soft samples.

Friction force microscopy (FFM) is another AFM measurement mode where the tip is in continuous contact with the sample surface[ii]. In the case of FFM, the lateral movement of the light beam reflected from the cantilever is detected. This signal is proportional to the tilting of the AFM needle and thus carries information about the friction force between the tip and the surface. The contact lateral friction force depends on the chemical composition of the surface. The tip tilt measurement can thus be used to map the chemical composition of the surface with nm resolution. Although a friction force microscope cannot be used to identify the chemical composition of a surface, it can be used to detect changes in chemical composition. This type of measurement is particularly useful if there are chemically distinct regions on a sample surface, such as chemically segregated regions or intentionally grown nanostructures. This detection scheme enables simultaneous measurement of topography and friction images. Today, AFM/FFM is widely used as a standard tool

to observe material surfaces.

In this study, in order to obtain surface morphology information, the dynamic force mode (DFM), which is a kind of non-contact measurement mode, was mainly used because of the higher resolution of the image that can be obtained by DFM than FFM. In DFM mode, a needle is also placed on a flexible cantilever, and the cantilever is vibrated by external oscillating force. As the AFM needle approaches the sample surface, the amplitude of the cantilever vibration decreases due to the interaction between the needle and the sample. The segmented photodetector detects the vibration amplitude, and a horizontal scan is performed while keeping the amplitude loss constant. Again, a topographic image can be obtained. The resolution of the system is determined by the diameter of the tip and it is routinely possible to achieve nm order spatial resolution. AFM is not limited to conducting samples, as is STM, and can be used in air, liquid, or vacuum. In this study, SPM9600 (Shimadzu) was used. SPM9600 can be used for both tapping mode and friction force measurements.

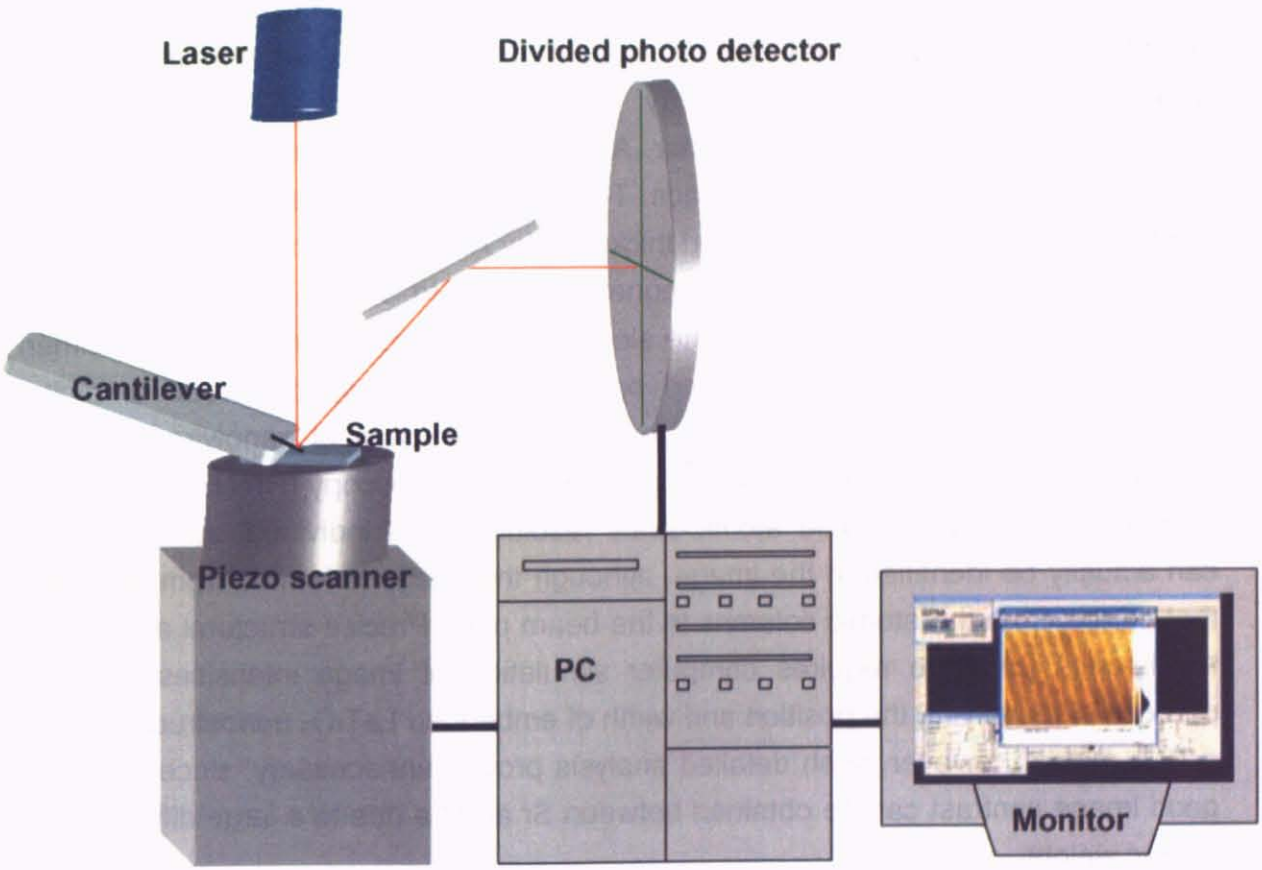

Fig.3-2-1 Essential parts of an Atomic force microscope

3-2-2 Transmission Electron Microscopy

Transmission electron microscopy (TEM) is one of the most important tools for atomic-scale microstructural characterization of materials. The biggest advantage of TEM over other techniques is the ability to look inside thin samples at an atomic resolution, thanks to the very short wavelength of high-energy electrons and the strong interaction between the electron beam and the charges inside a sample crystal. The schematic image of TEM system is shown in Fig.3-2-2.

To observe a cross-sectional image of a thin film sample, a thin specimen needs to be cut from the sample in the desired imaging direction. The samples used in this work were prepared in the following way. Two parts of a sample were glued together with the film surfaces facing each other. A slice was cut from the glued sample and grinding was used to obtain a thin slice. The sample was dimpled close to the glue layer and finally thinned to the desired thickness by Ar beam milling.

Conventional TEM uses electromagnetic lenses to focus the electrons into micrometer-order thickness beam. The electron beam passes through the specimen and the transmitted beam is focused on an imaging phosphor screen or digital camera. The images that were used to study the structure of nanowires required atomic-scale resolution, which is why high-resolution microscopy (HRTEM) was used. The HRTEM images provide atomic-scale resolution and individual atom columns can actually be identified in the image, although the image is formed from electrons that diffract from the atomic columns in the beam path. Precise structural analysis of the images therefore requires computer simulation of image intensities. For the purpose of identifying the position and width of embedded $LaTiO_3$ nanostructures in a $srTiO_3$ matrix, however, such detailed analysis proved unnecessary, since relatively good image contrast can be obtained between Sr and La due to a large difference in atomic weight.

Another TEM variation, which gives even better spatial resolution and also carries information about the chemical composition is the scanning transmission electron microscopy (STEM), which was also used in this study. In this type of instrument, the electron beam is focused into an extremely narrow beam, on the order of the width of a single atomic column. The transmitted electrons are detected with a movable detector at the bottom of the microscope column[iii]. STEM has two kinds of detection mode, which are called Higher Angle Annular Diffraction (HAADif) mode and Lower Angle Annular Diffraction (LAADif) mode. In HAADif mode, the electron detector is set higher angle to the annular center, while in LAADif mode, the detector is set lower angle to the annular center. When the electron beam interacts with heavy atoms, electron scatter to higher angles. Therefore HAADif is used to detect atomic weight contrast, essentially analyzing the chemical composition of a sample. LAADif is also

useful, since it carries information about lattice distortions. The HAADif mode was used in this study, since it more useful for imaging the chemical contrast in the vicinity of embedded nanostructures.

The TEM and STEM measurements of the heterostructure samples were done by Professor Takahisa Yamamoto and his students.

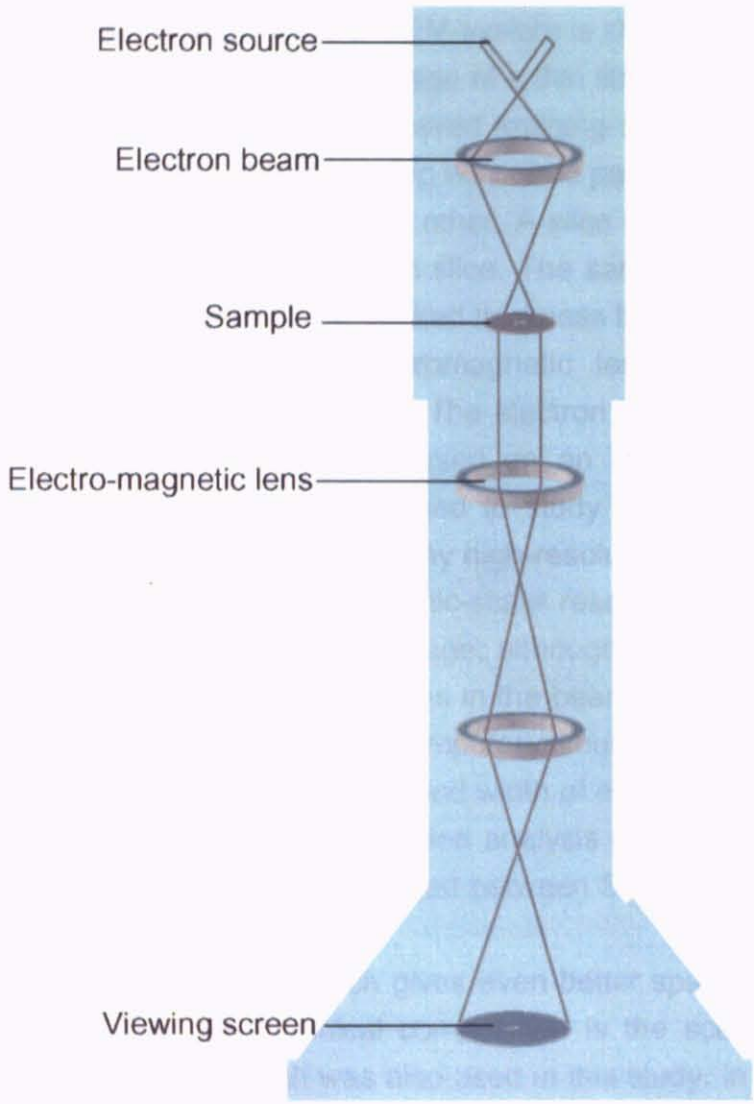

Fig.3-2-2 Schematic image of a TEM system

3-2-3 Electrical measurement on nanowires

In a nanowire sample, the resistance parallel to the wire direction is expected to be metallic behavior, while the resistance perpendicular to the wire direction should show insulating behavior. In order to measure the transport properties of both insulating and conducting samples, the measurement setups need to be different. Since the resistivity perpendicular to the wires is very high, it is only possible to measure the transport properties in a 2-point geometry current-voltage (IV) mode. The resistivity behavior along the wire direction should be measured in a four-point mode, since contact resistances can be of the same order of magnitude as the sample resistance, as shown in Fig.3-2-3-1.

In order to obtain Ohmic contacts with the embedded wire layer, titanium electrodes were evaporated on the sample surface. Titanium was deposited by electron beam evaporation through a metal mask that defined the shapes of the electrodes. The actual conducting wire structure is embedded inside the sample, covered with an insulating $SrTiO_3$ capping layer. Transport properties of the embedded wire layer cannot therefore be estimated precisely because the current path cannot be determined accurately.

However, titanium metal on $SrTiO_3$ acts as a very strong reducing agent. The reaction of a titanium metal electrode with the $SrTiO_3$ capping layer actually changes the capping layer from an insulating state to a metallic state. This transformation only occurs in regions covered by the titanium electrodes and then the electrode size can therefore be accurately determined. After evaporating titanium, Al wires were bonded to the electrodes, as shown in Fig.3-2-3-2. The bonding wires connected the sample pads to the ceramic chip carrier package, which was used in the low-temperature electrical measurement system.

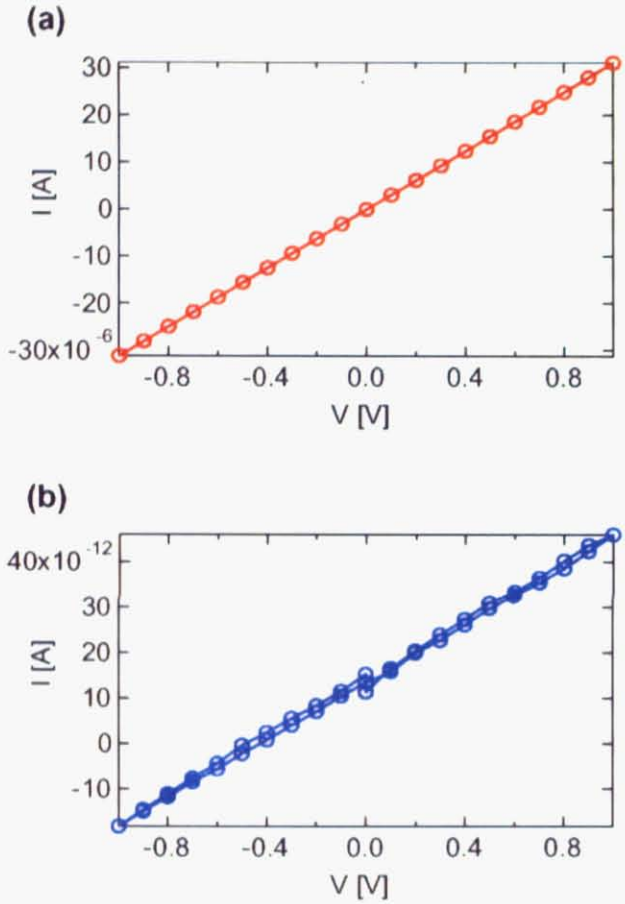

Fig. 3-2-3-1 A two-point I-V curves of $LaTiO_3$ wires measure (a) parallel to the wires and (b) perpendicular to the wires.

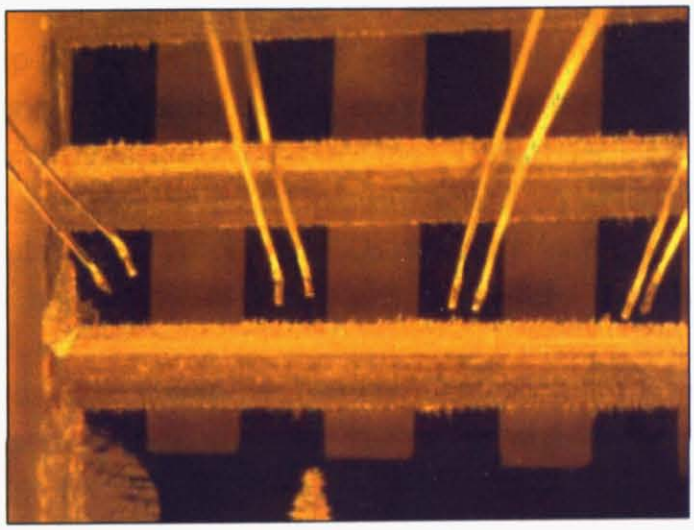

Fig. 3-2-3-2
A photo of the titanium electrodes on the sample surface. The aluminum bonding wires are also visible.

References

[i] T. Sulchek et al., Rev. Sci. Instrum., **73**, 2928 (2002)
[ii] G. Meyer et al., Appl. Phys. Lett., **57**, 2089 (1990)
[iii] B. Fultz and J. M. Howe: Transmission Electron Microscopy and Diffractometry of Materials (Springer, Germany 2001) pp 63-66

3-4 Fabrication and characterization of embedded $LaTiO_x$ nanowires

As discussed in the previous section, $LaTiO_3$ films that were capped with $SrTiO_3$ showed metallic behavior. As a result of using an $SrTiO_3$ capping layer, an embedded LTO (113) phase appeared to be stable even after post annealing and the samples still showed metallic conductivity after annealing. My next target was to fabricate conducting $LaTiO_3$ nanowires embedded in an $SrTiO_3$ matrix. If successful, such wires would show anisotropic in-plane transport properties.

In preparation for this experiment, the first step was to determine the temperature range where step-flow growth of $LaTiO_3$ is possible. It was also necessary to determine how long it takes for $LaTiO_3$ atoms to migrate to the step edges at an oxygen background pressure of $1x10^{-6}$ Torr. Typical RHEED specular intensity oscillation behavior during step-flow growth of $LaTiO_3$ is shown in Fig.3-4-1. In addition to this data, direct proof of $LaTiO_3$ nanowire formation along the substrate step edges was sought by AFM analysis of sample surface morphology and composition.

The first samples were grown by manually controlling the firing of the deposition laser pulses at a sample temperature of 1100 °C. After firing a single pulse, the time that was needed for the RHEED intensity to recover to the initial level was measured. The time is the surface relaxation time, determined by the surface diffusion rate (temperature) and the average terrace width. After waiting until the RHEED intensity recovered, the temperature was decreased to 1050 °C and the relaxation time was measured again in the same way. The same measurements were also done at 1000 °C, 950 °C and 900 °C. Finally, at 900 °C the RHEED intensity no longer recovered completely. This suggests that a 900 °C substrate temperature is not high enough for pure step-flow growth. Fig.3-4-2 shows the temperature dependence of measured relaxation times. Based on this result, it was concluded that if $LaTiO_3$ wires are deposited at 1000 °C, a 10 second delay between deposition pulses is long enough for the RHEED intensity, and thus also the surface morphology, to recover completely. That is to say, if $LaTiO_3$ is deposited at 1000 °C, a pure step-flow growth mode emerges and a step-decorating structure can be formed at laser pulse repetition rates of 1 Hz or less.

Fig.3-4-3(a) shows the experimental procedure of fabricating embedded $LaTiO_3$ nanowires. After pre-annealing the substrate to obtain a regular step-and-terrace surface morphology, 0.2 u.c. of $LaTiO_3$ was deposited at 1000 °C at a laser repetition rate of 1 Hz. The substrate temperature was reduced immediately after deposition to 700 °C by switching the heating laser current so that interdiffusion between the

$LaTiO_3$ layer and the $SrTiO_3$ substrate and subsequent $SrTiO_3$ capping layers could be prevented. After that a 100 Å-thick $SrTiO_3$ capping layer was deposited at 700 °C at a laser repetition rate of 2 Hz. In these experiments, the growth rate of LTO was approximately 60 pulses per monolayer, which was relatively low, but made it easier to control the amount of deposited material. The oxygen pressure was fixed during deposition at $1x10^{-6}$ Torr. After deposition, the samples were post-annealed at 400 °C for 6 hours in a furnace in air in order to compensate oxygen vacancies in the $SrTiO_3$ capping layer and possibly the substrate. Fig.3-4-3(b) shows a typical RHEED intensity variation, which clearly shows the signatures of step-flow growth during the deposition of LTO nanowires and layer-by-layer growth during the deposition of the $SrTiO_3$ capping layer. Fig.3-4-3(c) shows AFM topography and phase shift images (1 μm x 1 μm) of the capping layer surface. A clear step-and-terrace surface, reflecting the original substrate surface was observed. The phase shift image showed no chemical contrast on the capping layer surface.

At first, a wire sample was fabricated at 1000 °C for further AFM study. This sample did not have a $SrTiO_3$ capping layer. This sample was grown at a constant laser pulse repetition rate of 1 Hz. The number of deposition pulses was selected so that the estimated $LaTiO_3$ film coverage was 0.2 unit cells. This coverage was expected to form a wire structure that covers one fifth of each substrate terrace. The AFM topography and phase images measured in the center part of the sample are shown in Fig. 3-4-4(a). There is no contrast except for the abrupt jumps at the step edges when measurements were made in a region covered by wires. The lattice constants of $LaTiO_3$ and $SrTiO_3$ are almost equal. In this case, the substrate was terminated by the TiO_2 plane and the $LaTiO_3$ termination on a TiO_2-terminated $SrTiO_3$ is also a TiO_2 plane (Fig.3-4-4(b)). That is probably why no chemical contrast was seen in the phase shift image, except for the abrupt jumps at the step edges.

In order to verify the presence of nanowires in this sample, an alternative technique was needed. In addition to AFM, therefore, transmission electron microscopy (TEM) and scanning TEM measurements were made of the wire sample. Fig.3-4-5(a) shows a schematic diagram of the sample used for cross-sectional TEM imaging. The corresponding TEM image is shown in Fig.3-4-5 (b), where the contrast of the embedded wires can be clearly seen. For better imaging of the single unit cell structures, scanning TEM images were also taken, as shown in Fig. 3-4-5 (c). This sample had a STO capping layer, so the $LaTIO_3$ wires were bounded on both sides by $SrTiO_3$. The cross-sectional wire structure can be seen both in TEM and STEM images. The left-hand-side plot of STEM image shows an integrated intensity profile, where higher intensity corresponds to rows of heavier atoms. Oxygen is too light to be seen in these images. The various peaks and the characteristic intensities can be assigned to rows of Sr, Ti, and La. Among these elements, La is the heaviest,

followed by Sr, and Ti, which is the lightest. Therefore, the strongest intensity corresponds to La, and the weakest must be Ti, while Sr layers have intermediate intensity, as drawn in the Fig.3-4-5 (c). These TEM and STEM images show very sharp La contrast, indicating that there is minimal vertical diffusion of La into $SrTiO_3$, even after the capping layer was deposited onto the wires.

In order to eliminate the possibility of position dependence, resistance for various directions was measured in a small region of a sample. Aluminum wires were bonded to the sample surface as shown in Fig.3-4-6 (a). The distance between each bonding pad was 0.3 mm. The bonding positions were selected so that resistance could be measured along the wire direction and also in a direction perpendicular to the wires. The wire directions was known from the AFM image of the sample surface, which is also shown in Fig.3-4-6 (a). The directional dependence of sheet resistance is shown in Fig.3-4-6 (b). The angle is measured between the measurement direction and the direction of the surface steps. Although the resistance measured at 0° appears to be the lowest, the variation of resistance is less than 40%, which can be neglected because there may be other sources of error in the resistance values.

It was obvious from these experiments that it is not possible to obtain anisotropic conductivity by simply changing the wire growth parameters, since the TEM images showed that at least structurally, high-quality wires were present in the sample and metallic conductivity was observed in the sample. The likely reason for not observing in-plane anisotropy was that the wires were shorted, probably because of low residual resistivity of the terraces.

I therefore examined ways of modifying the wire structure by converting the usual $SrTiO_3$ substrate-terminating layer from TiO_2 to a SrO layer. A schematic model of a $LaTiO_3$ nanowire on a SrO-terminated $SrTiO_3$ surface is shown in Fig. 3-4-7 (a). The structures is essentially similar to the case shown in Fig. 3-4-4 (b), except for switching the top and bottom interfaces. The experimental procedure of fabricating a sample is shown in Fig. 3-4-7 (b). The SrO buffer layer was deposited at 550 °C in $1x10^{-6}$ Torr of oxygen. The substrate termination was controlled by atomic-layer growth of SrO thin films. The number of SrO deposition pulses was selected so that the estimated film coverage was 1 u.c. or 0.5 u.c., as measured from the RHEED oscillation period. The expected coverages were 100% and 50% of a substrate terrace.

After SrO deposition, it was necessary to increase the substrate temperature from 550 °C to 1000 °C, where $LaTiO_3$ grows in step-flow mode and wire structures can be formed. The effect of high-temperature annealing of thin SrO layers deposited on a $SrTiO_3$ substrate surface was therefore studied in detail. After SrO growth, samples were annealed at various temperatures up to 1000 °C, which is the temperature where the actual $LaTiO_3$ nanowire structure is grown.

Fig.3-4-8 shows the various sample fabrication workflows that were used to study the annealing effects on the surface morphology of the SrO buffer layer. In all cases the samples were pre-annealed and SrO was deposited at 550 °C. In the first sample, the temperature was increased immediately after the end of the deposition to 1000 °C. The sample was annealed for 10 minutes, cooled down to room temperature and imaged by AFM. The temperature profile and the resulting AFM image are shown in Fig.3-4-8(a). The formation of islands on the sample surface was observed. In the next sample, the deposition was carried out in the same way, but the sample was briefly cooled down before performing the same 10 minutes 1000 °C annealing step. The AFM image of this surface, shown in Fig.3-4-8 (b) had a high density of holes in the terraces. It was obvious that the migration of SrO is strongly influenced by the annealing procedure, but the surface of this sample was not suitable for wire fabrication.

The process was finally modified by cooling the sample after deposition and exposing the sample to air for immediate AFM observation. The sample was subsequently re-introduced into the chamber and annealed the same way as the previous samples. The temperature profile is shown in Fig.3-4-8 (c). After the 10-minute anneal, a meandering surface morphology was observed. This structure is similar to the morphology seen in annealing as-delivered commercial substrates. The sample was therefore annealed for an additional 60 minutes, after which a nearly perfect step-and-terrace surface with straight step edges was observed in AFM images (Fig.3-4-8 (c)).

This series of experiments showed that cooling the sample after deposition and possibly exposing the sample to air is needed to obtain a flat SrO buffer layer that is suitable for nanowire fabrication.

Fig. 3-4-9 (a) shows the topography of a 1 u.c. SrO film on $SrTiO_3$ after annealing at various temperatures for 10 minutes or 1 hour. The annealing temperature and time were *a*.0 min., *b*. 800 °C 10min., *c*. 800°C 1hour, *d*. 900°C 1hour and *e*. 1000°C 1hour. In some images, the meandering morphology can be seen. A similar annealing experiment was done after 0.5 u.c. SrO deposition. Fig. 3-4-9 (b) shows topography of the 0.5u.c. SrO film on $SrTiO_3$. Annealing temperature and time was *a*. 900°C 10min. and *b*. 1000°C 1hour. In this case, an island structure emerged at first but disappeared after annealing at 1000°C for 1 hour. These result showed that the surface morphology still changed during annealing after SrO deposition even though the samples had already been annealed once to obtain straight steps. The conclusion therefore was, that a second high-temperature annealing step is needed between SrO deposition and $LaTiO_3$ wire deposition to reconstruct a step-and-terrace substrate surface.

A 0.2 u.c. $LaTiO_3$ wire layer was grown after SrO deposition and 1000 °C 1 hour

annealing, which was necessary for reconstructing the substrate surface. The $LaTiO_3$ wire fabrication was done at 1000 °C at a laser repetition rate of 0.01 Hz. This rate is long enough to recover the RHEED intensity after each pulse. Relaxation time measurement of RHEED had been done beforehand. From this measurement, the relaxation time was found to be 50 seconds on a surface that had been coated with a 1 u.c. SrO layer and 10 seconds on a surface with a 0.5 u.c. SrO buffer layer. The deposition pulse rate of 0.01 Hz was used in the $LaTiO_3$ wire deposition, since this allowed for sufficient recovery time in both cases.

Fig.3-4-10 shows the AFM topography and phase image of the $LaTiO_3$ wires on 1 u.c. and 0.5 u.c. SrO-buffered $SrTiO_3$. A somewhat unexpected AFM topographic image was seen in both samples, since a wire-shaped contrast was visible in the topography images. The lattice constants of $SrTiO_3$ and $LaTiO_3$ are almost the same and no height contrast would therefore be expected.

It is not clear why this structure was observed in topography, but such contract was only visible in sample where nanowires had been deposited. Phase images showed good contrast between the $LaTiO_3$ wires and the $SrTiO_3$ substrate terraces both in the sample with 1 u.c. and 0.5 u.c. SrO buffer layer, as expected.

The deposition of the STO capping layer and ex-situ post annealing were done in the same way as previously described.

The structure of a wire grown on a 1 u.c. SrO buffer layer was studied by STEM in order to compare the wire structure to the sample where wires were grown directly on a TiO_2 -terminated $SrTiO_3$ substrate. Fig.3-4-11 shows a STEM image of a $LaTiO_3$ wire deposited on the SrO buffer layer. This STEM image also shows a sharp La contrast. This shows that La atoms did not diffuse along the c-axis direction, even after the capping layer was deposited onto the wires as in the case of the wires on the substrate with no SrO buffer layer.

The transport properties of the LTO wires were again measured in parallel (//) and perpendicular ($\perp$) to the LTO nanowire direction both on 1 u.c. and 0.5 u.c. SrO buffer layers. As far as the 1 u.c. SrO sample is concerned, the sheet resistance in the parallel direction ($R_{//}$) was 840 kΩ/sq and sheet resistance in the perpendicular direction was 2.3 MΩ/sq. The largest ratio of resistances observed in the sample with a 1 u.c. buffer layer never exceeded 4.8. In contrast, $LaTiO_3$ wires on the 0.5 u.c. SrO buffer remarkably showed much lower $R_{//}$ value compared to the $R_{\perp}$ value. The sheet resistance ratio on the 0.5 u.c. SrO-buffered substrate was 6.1×10^5. Both were measured under room light exposure. In order to eliminate the effect of photo-induced carriers, the 0.5 u.c. SrO sample was kept in darkness, the ratio of anisotropy started to increase over time. The $R_{\perp}$ value increased from 7.2×10^{10} to 1.3×10^{12} and the $R_{//}$ value increased from 3.9×10^4 to 5.0×10^4. The final in-plane anisotropy reached 2.6×10^7. (Fig.3-4-12) This implies that transport in the

perpendicular direction to LTO nanowires was mostly derived from photocarrier generated in the $SrTiO_3$ surface layer. On the other hand, a relatively small photoconductive effect in the parallel direction represents transport along the heavily doped $LaTiO_3$ nanowires, which have a very large carrier concentration and are thus less sensitive to photocarriers.

After eliminating the effect of photo-induced carriers, temperature dependence of the sheet resistance was measured. Both in $R_{//}$ and $R_{\perp}$ showed metallic behavior except for at the lowest temperatures of $R_{\perp}$. (Fig.3-4-13 (a))

I mentioned above that transport in the perpendicular direction to the $LaTiO_3$ nanowires was mostly derived from photocarriers generated in the $SrTiO_3$ layer and showed a relatively small photoconductive effect in the parallel direction. Further consideration supported this transport model. Fig.3-4-13 (b) shows the sheet resistance data, re-plotted as a function of square of temperature. Sr doped $LaTiO_3$ ($Sr_{1-x}La_xTiO_3$) is known to show quadratic temperature dependence of resistivity that represents the strong electron-electron scattering process, which seems to predominate the electron-phonon scattering process[i]. The re-plotted $R_{//}$ shows a good linear dependence with T^2. This fact also indicates that charge transport occurred along the $LaTiO_3$ nanowires and neighboring carrier-doped $SrTiO_3$ layers. On the other hand, the $R_{\perp}$ doesn't have a linear dependence and has a relatively large R.R.R. value. This behavior appears to be derived not from the $Sr_{1-x}La_xTiO_3$ system but rather from the electron-doped $SrTiO_3$[ii]. In this way, the transport properties of the $LaTiO_3$ nanowires can be identified not only by the very large anisotropy but also by the shape of the ρ-T curves measured in each direction.

AFM and TEM measurements indicated that the wire structure could be obtained by controlling the temperature and the laser repetition rate so that pure step-flow growth is obtained. The STEM measurements confirmed that La atoms are not diffusing along the c-axis direction. Although the wire structure was obtained both on 1 u.c. and 0.5 u.c. SrO buffer layers, the anisotropy of conductance, which should be a characteristic of the conducting wires, was considerably different. These results suggest that changing the surface termination layer is not the critical step needed for anisotropic wire conductivity. It is more likely that SrO deposition compensated the Sr vacancies that were generated during initial substrate annealing to obtain straight steps and this prevented Lanthanum diffusion into the substrate surface. Excess Sr may prevent $LaTiO_3$ from surface migration in step-flow growth, resulting in small anisotropy of conductance on the 1 u.c. SrO layer.

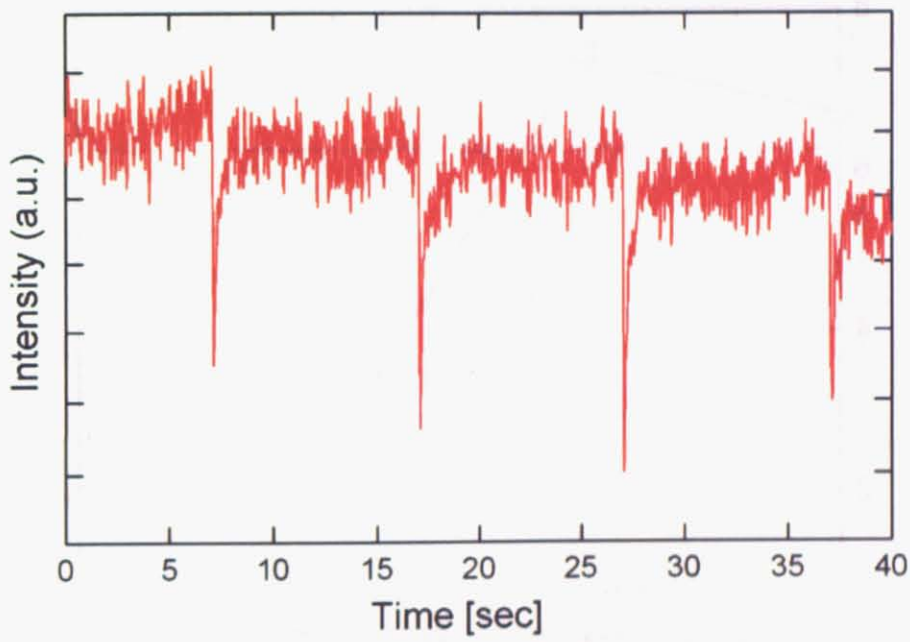

Fig. 3-4-1
Typical RHEED specular intensity behavior during step-flow growth of $LaTiO_3$ on $SrTiO_3$ at a temperature of 1000 °C and an oxygen pressure of $1x10^{-6}$ Torr.

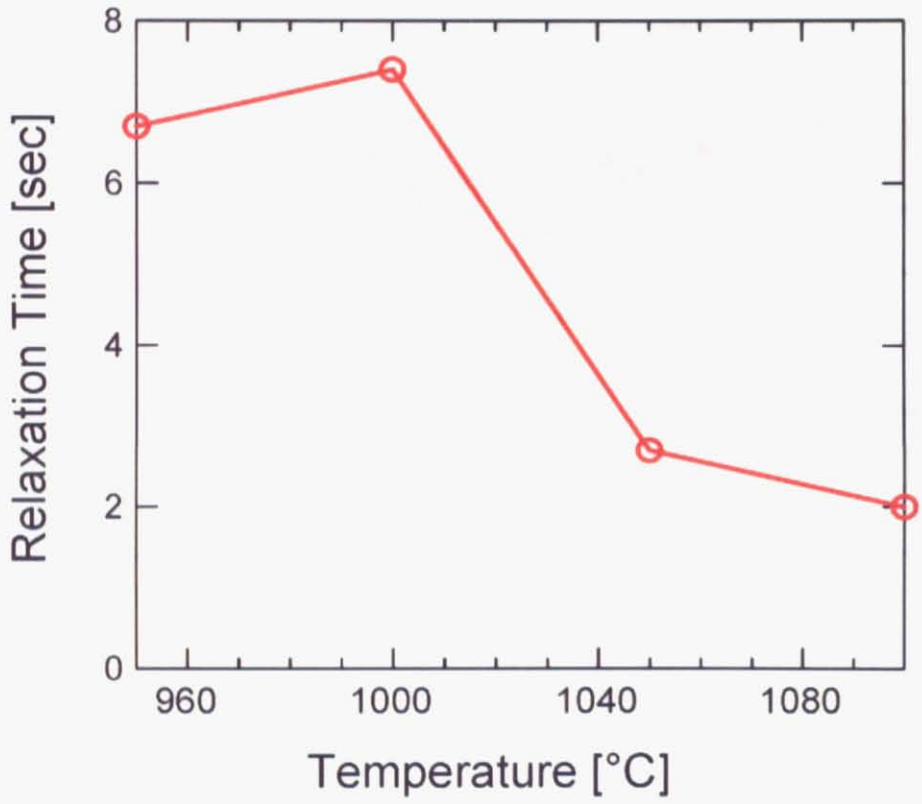

Fig. 3-4-2

Temperature dependence of relaxation times of step-flow growth of $LaTiO_3$ at an oxygen pressure of $1x10^{-6}$ Torr (measured on TiO_2 terminated STO substrate)

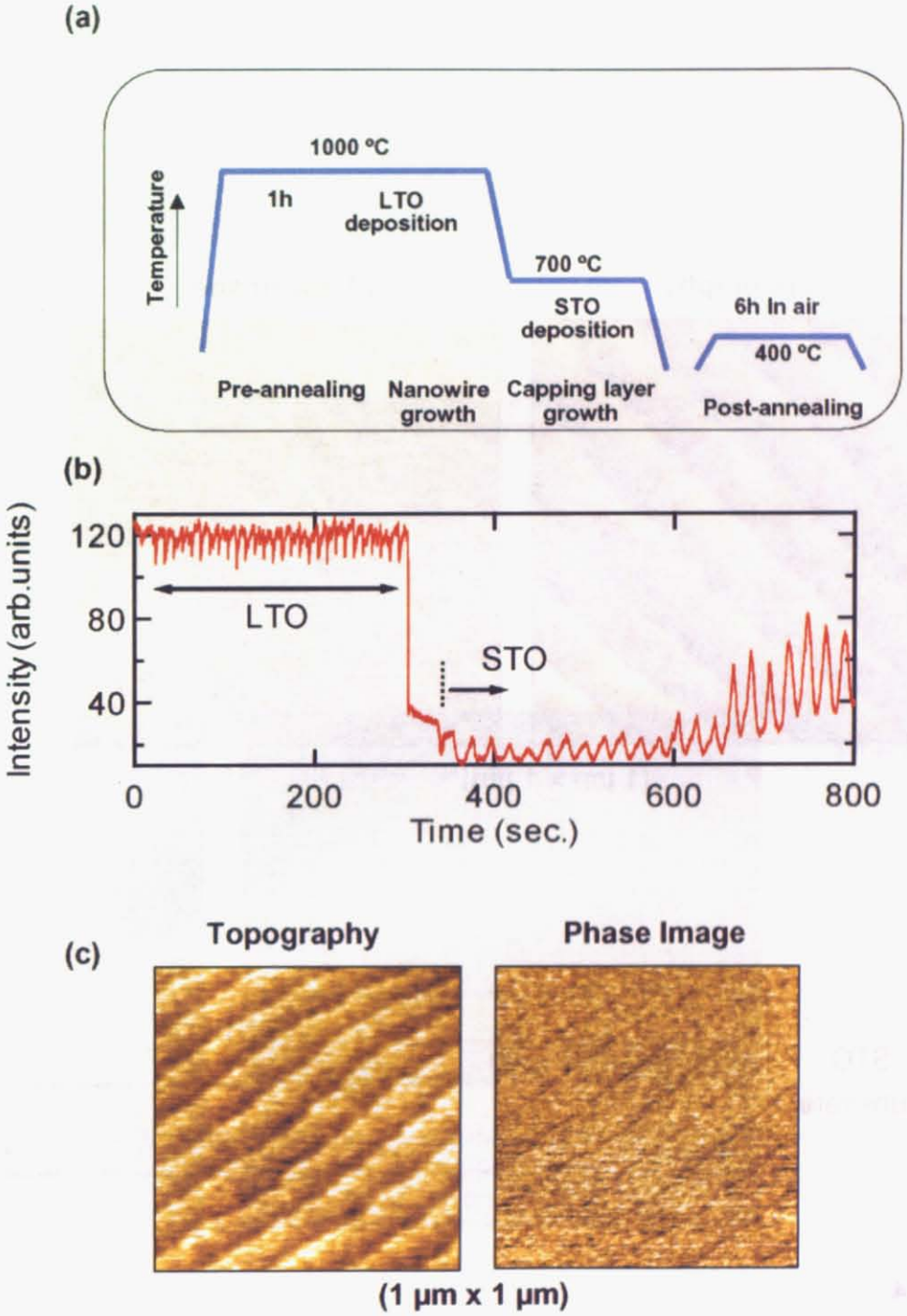

Fig. 3-4-3

(a) Experimental procedure of fabricating embedded $LaTiO_3$ nanowires

(b) Typical RHEED oscillation of fabricating embedded $LaTiO_3$ nanowires

(c) AFM topography and friction image taken on the $SrTiO_3$ cap layer

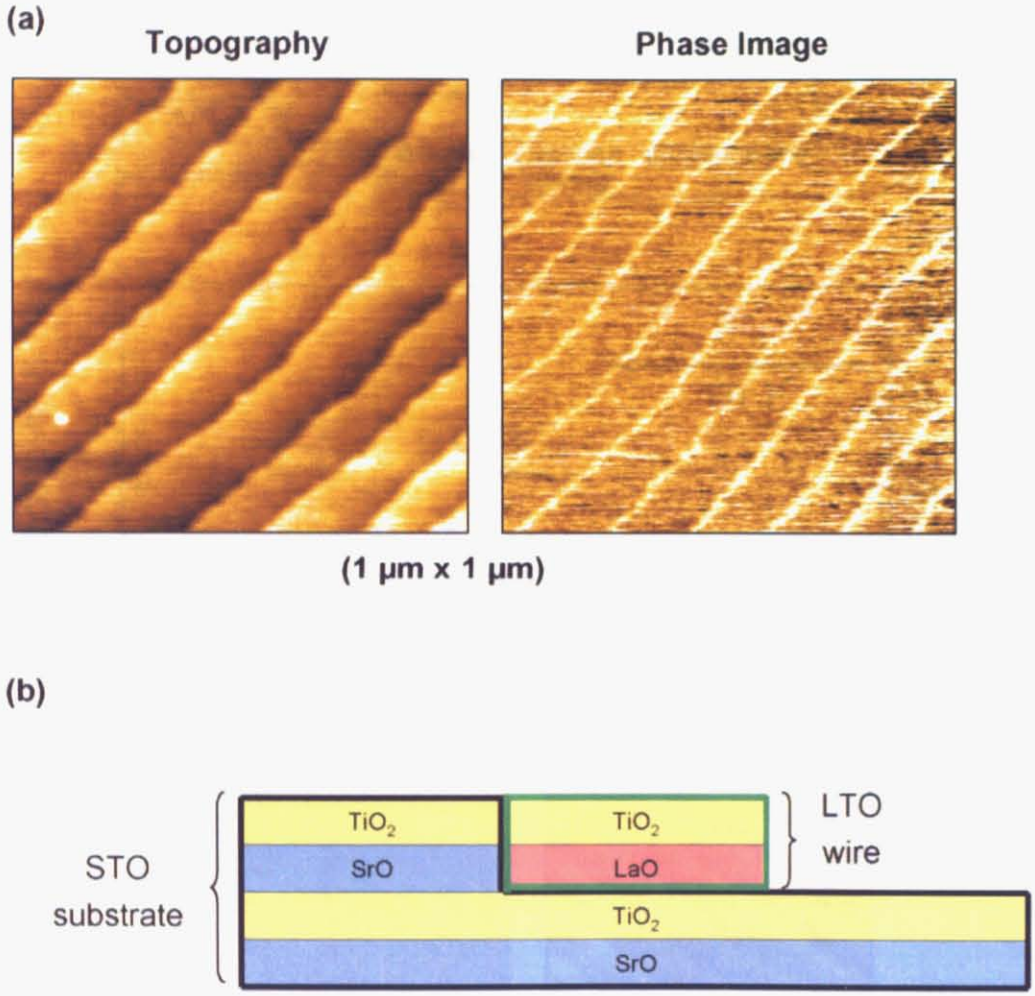

Fig. 3-4-4

(a) Topography and phase image of a $LaTiO_3$ wire structure deposited on a $SrTiO_3$ substrate. (b) Schematic model of an embedded $LaTiO_3$ layer on TiO_2 terminated $SrTiO_3$.

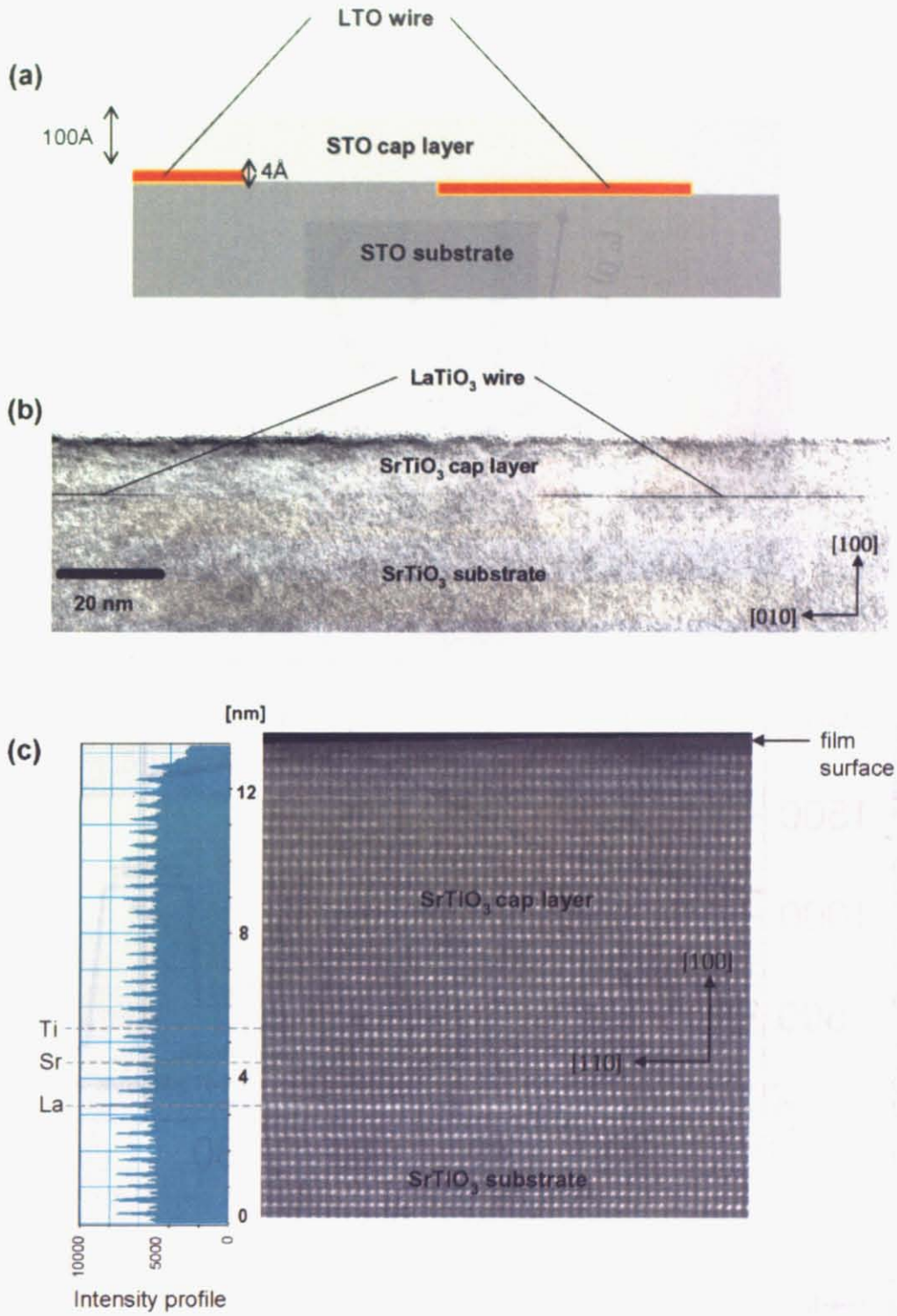

Fig. 3-4-5

(a) Cross-sectional schematic of embedded $LaTiO_3$ nanowires in a $SrTiO_3$ matrix. (b) Cross-sectional TEM image of the embedded $LaTiO_3$ nanowires, surrounded by the $SrTiO_3$ matrix. (c) Cross-sectional STEM image of a single $LaTiO_3$ nanowire in $SrTiO_3$.

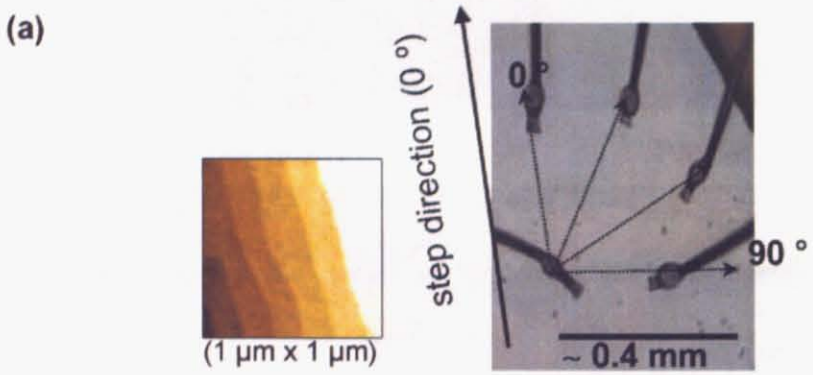

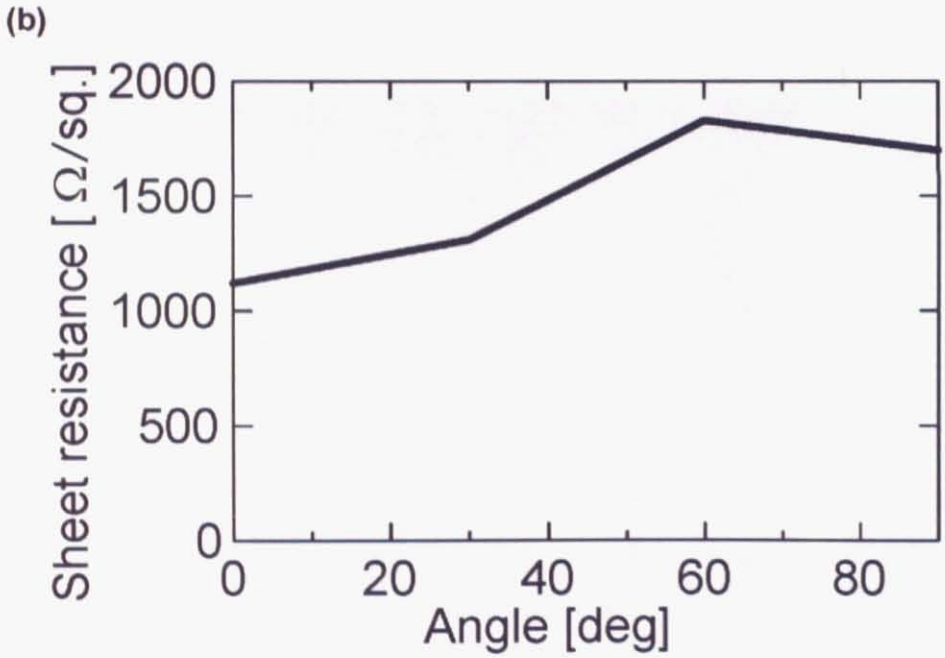

Fig. 3-4-6

(a) Photo of Al wire bonded substrate for electric measurements

(b) Angle dependence of sheet resistance on LTO wires

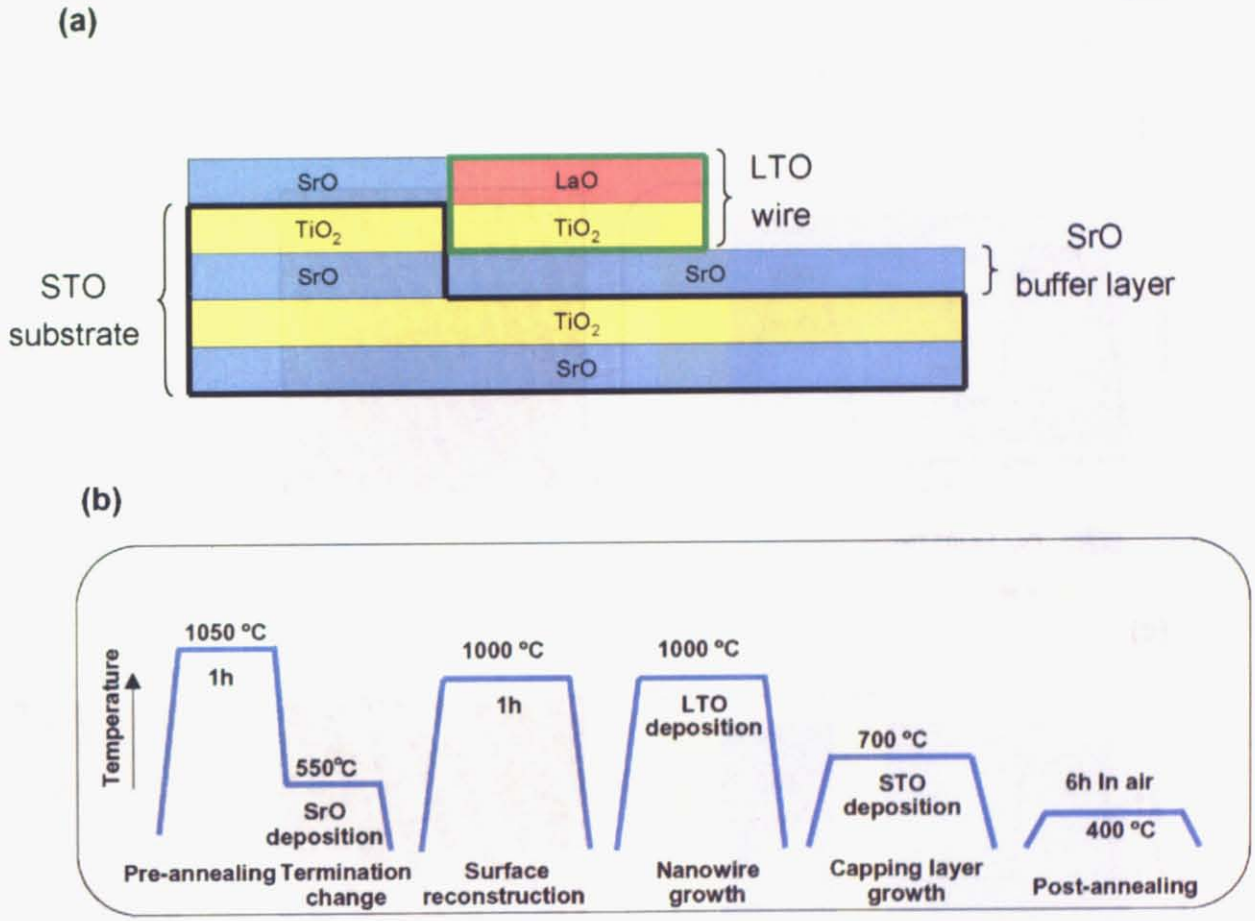

Fig. 3-4-7
(a) Schematic model of a $LaTiO_3$ wire on SrO-terminated $SrTiO_3$. (b) Experimental procedure of fabricating embedded LTO nanowires on an SrO-terminated substrate.

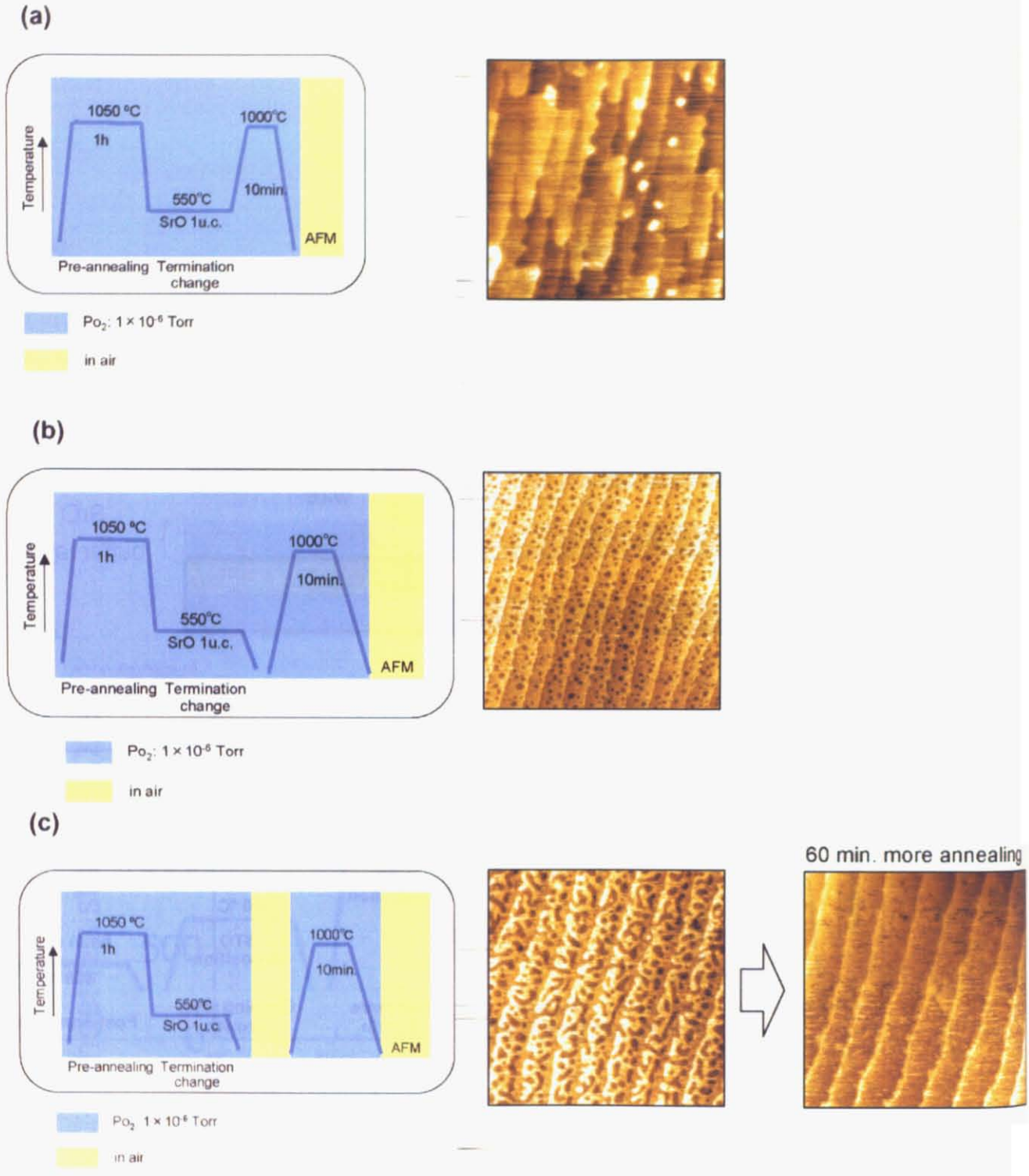

Fig.3-4-8

Process flow diagrams of SrO buffer layer fabrication and AFM images observed after annealing the buffer layers. (a) Sample was annealed immediately after deposition, (b) sample was briefly cooled before annealing, and (c) the sample was exposed to air before final annealing.

(a)

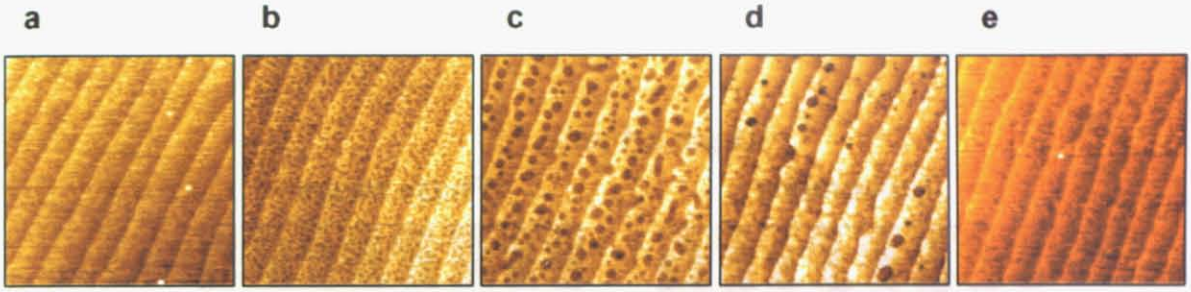

(b)

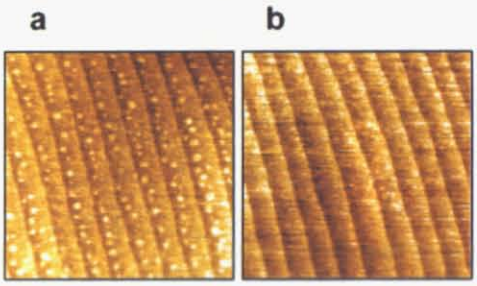

Fig. 3-4-9
(a) Topography of a 1 u.c. SrO film on $SrTiO_3$ (1μm×1μm)
Annealing temperatures and times are

a. 0 min.
b. 800 °C 10 min.
c. 800 °C 1 hour
d. 900 °C 1 hour
e. 1000 °C 1 hour

(b) Topography of a 0.5 u.c. SrO film on $SrTiO_3$ (1μm×1μm)
Annealing temperatures and times are

a. 900 °C 10 min.

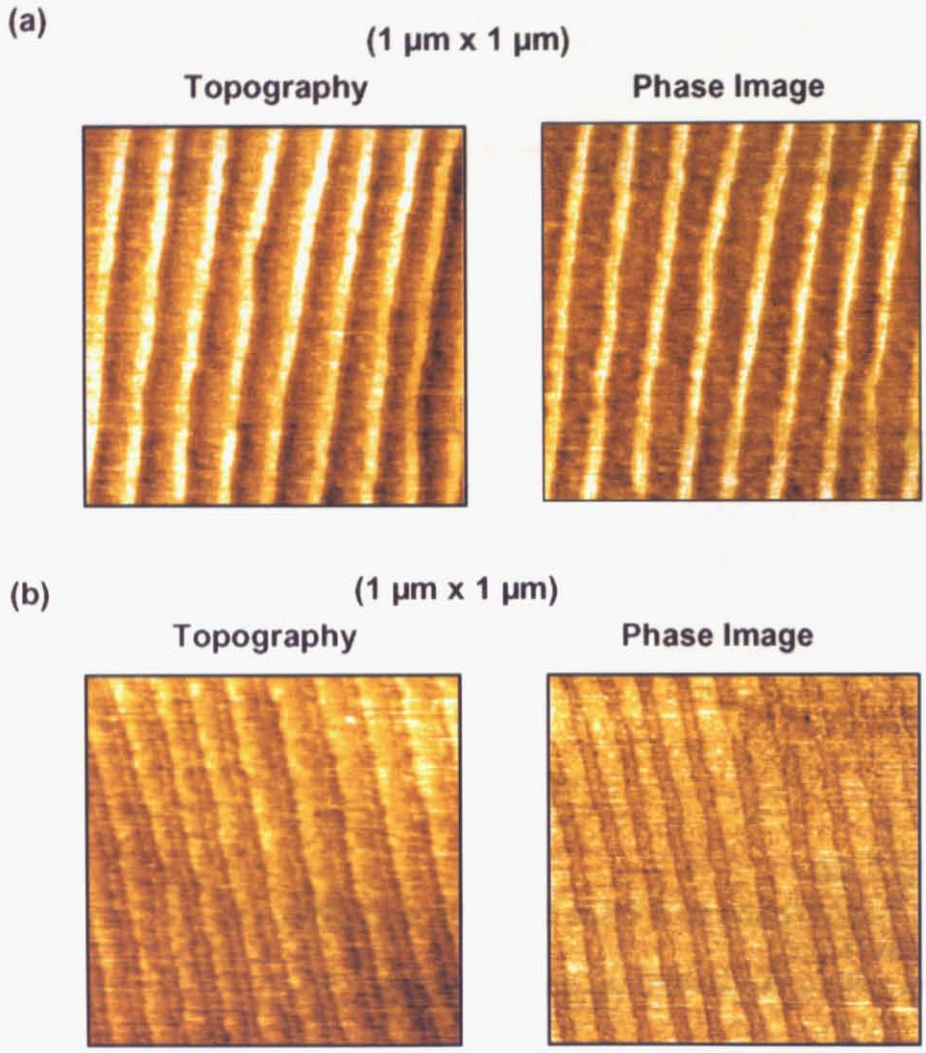

Fig. 3-4-10
(a) AFM image of $LaTiO_3$ wires on SrO-buffered $SrTiO_3$ substrate surfaces. The buffer layer coverage was 1 u.c. in (a) and 0.5 u.c. in (b).

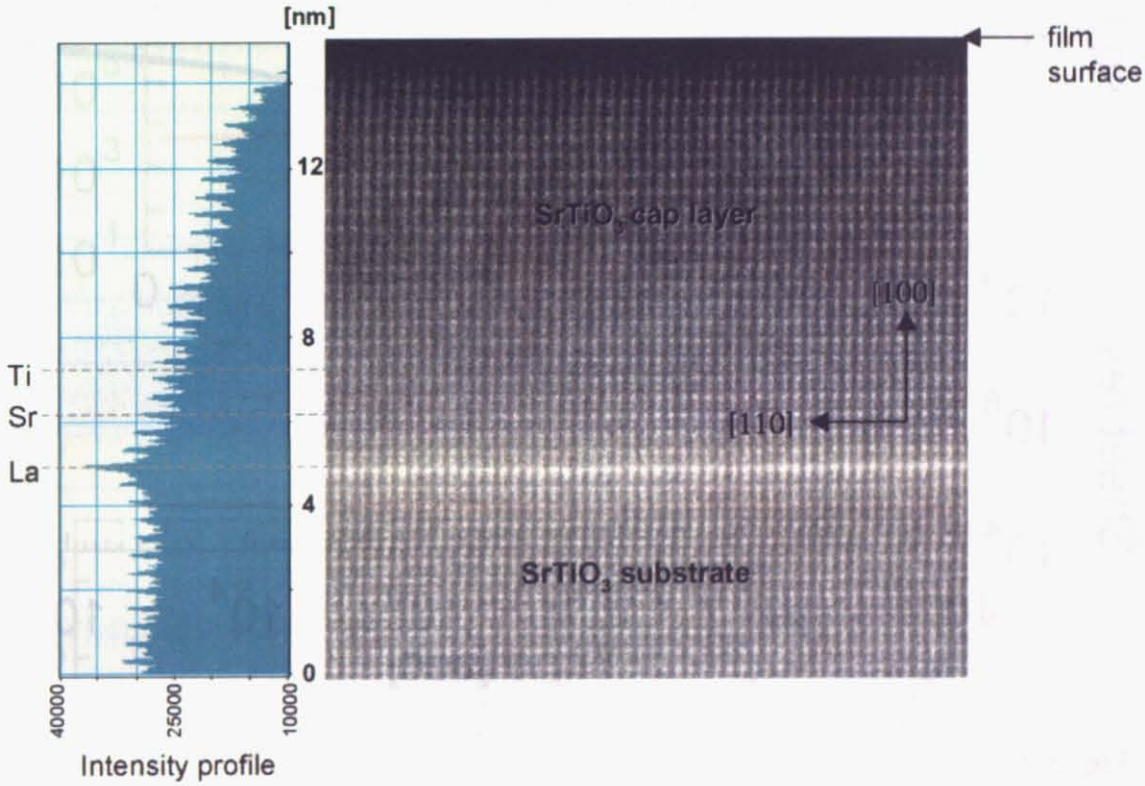

Fig. 3-4-11
Cross-sectional STEM image of $LaTiO_3$ nanowires in a $SrTiO_3$ matrix in which the $SrTiO_3$ substrate has a 1 u.c. SrO buffer layer.

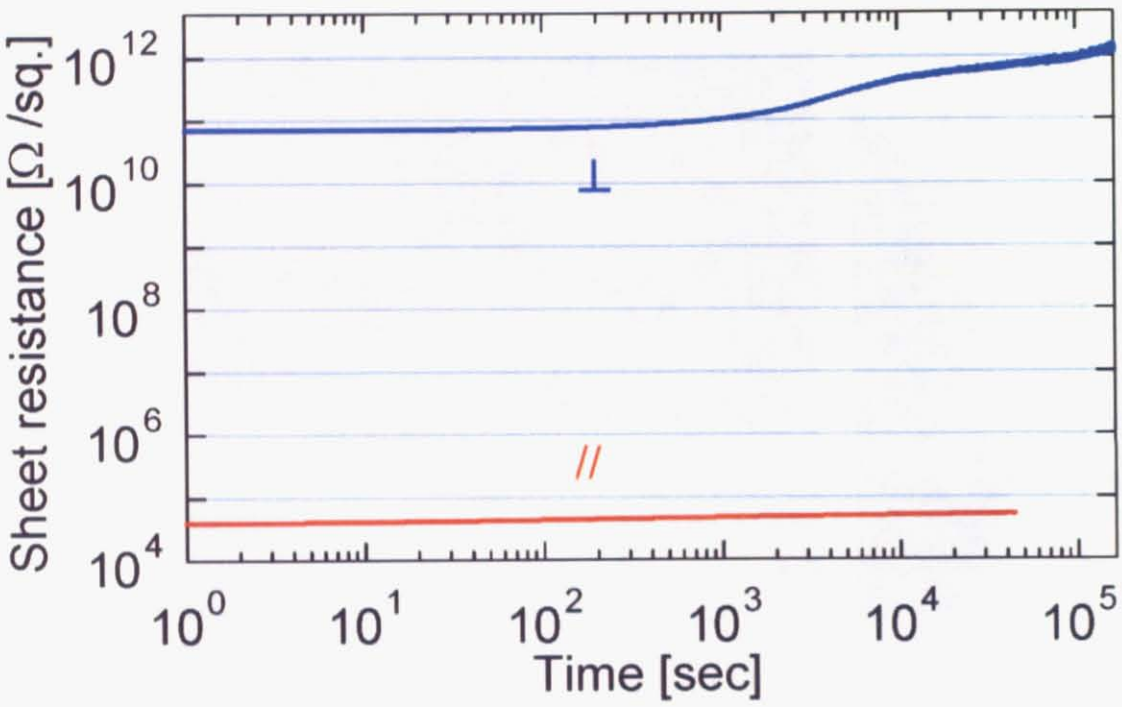

Fig. 3-4-12
Time dependence of sheet resistance measured at room temperature in parallel (//) and perpendicular (⊥) to nanowires

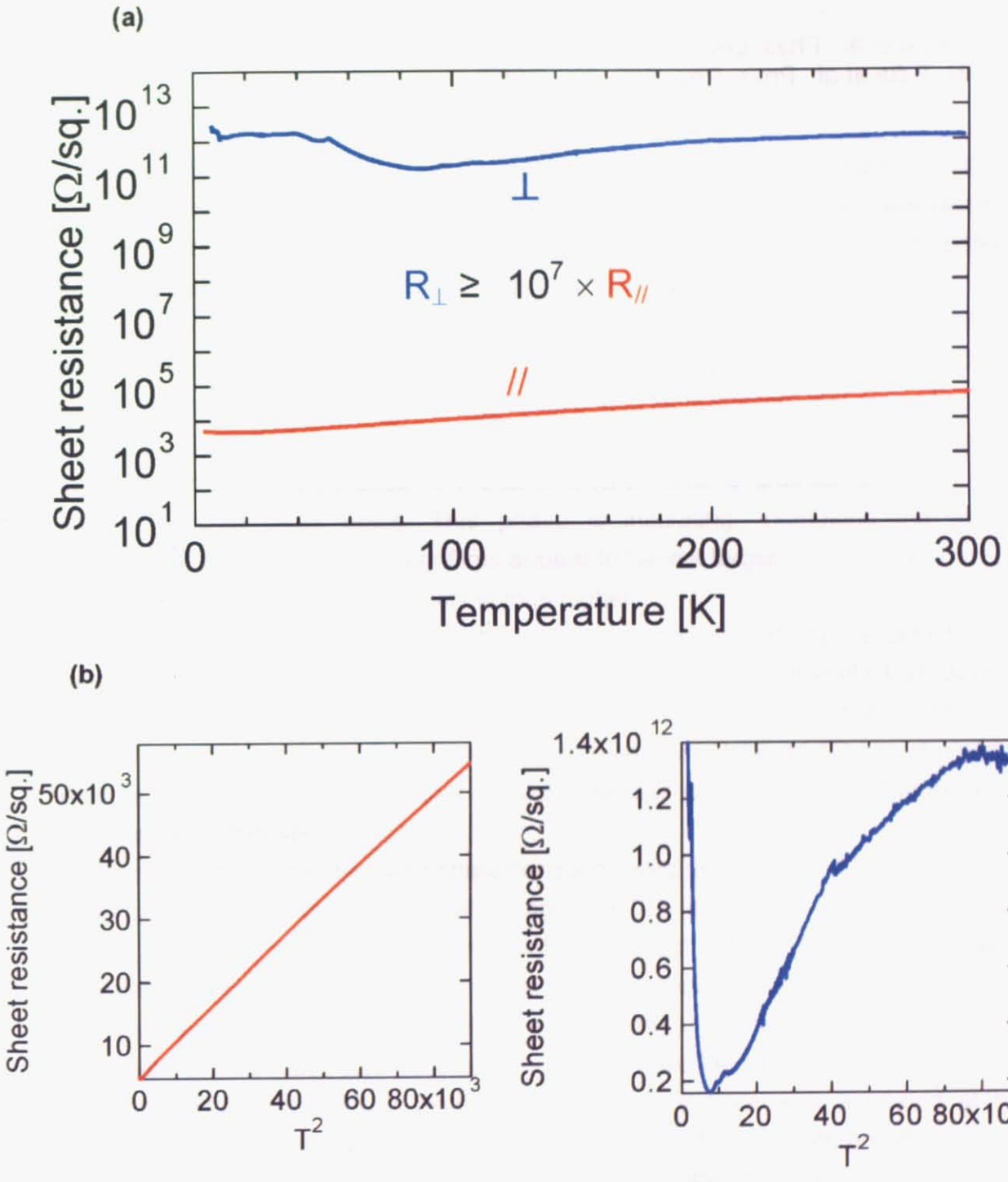

Fig. 3-4-13

(a) Temperature dependence of the sheet resistance

(b) Sheet resistance data re-plotted as a function of square of temperature

References

i Y. Tokura et al., Phys. Lev. Lett. 70 (1993) 2126
ii O. N. Tufte et al., Phys. Rev., 155, 796 (1967)

Chapter 4

Summary and Conclusions

In Chapter 1, the advantages of using perovskite transition metal oxides for nanostructure and heterostructure design were introduced. I also described the usefulness of nanowires for understanding heterointerface formation and for potential novel devices.

In chapter2, I described the optimization of the fabrication conditions of thick epitaxial metal oxide films. The ultimate goal of this study was to fabricate conductive $LaTiO_3$ nanowires. Transport measurements of thin films showed that as the thickness of the $LaTiO_3$ layer was reduced, the resistivity decreased. This unexpected behavior could be understood by assuming that in thicker films a gradual formation of the $La_2Ti_2O_7$ phase takes place. This phase is insulating, increasing the average resistivity of the films. The thicker films appear to have a larger proportion of the (227) phase, and the calculated resistivity is thus higher.

Measuring transmittance around 1800nm, which corresponds to the density of the free carriers in the film was used to estimate the fraction of the metallic $LaTiO_3$ phase in ultra-thin samples. Assuming that absorption occurs in the film, the transmittance should increase in thinner films. However transmittance data of LTO film showed the reverse behavior. This means that as film thickness became thinner, the density of free carriers increased.

The nanowire preparation and characterization was described in Chapter 3. $LaTiO_3$ nanowires were grown on atomically smooth $SrTiO_3$ substrates in step flow growth mode. $LaTiO_3$ wires on TiO_2 terminated $SrTiO_3$ substrate didn't show the expected in-plane anisotropy of conductance. I therefore examined ways of modifying the wire structure by converting the usual $SrTiO_3$ substrate-terminating layer from TiO_2 to a SrO layer. $SrTiO_3$ substrates were buffered with a 1 unit cell or a 0.5 unit cell SrO layer and the surface was briefly exposed to air. This surface was annealed at high temperature to produce a stable and insulating surface for nanowire growth

The $LaTiO_3$ nanowires were grown on $SrTiO_3$ substrates that had been coated with fractional SrO layers. The wires were also capped with a $SrTiO_3$ film. Such samples showed strongly anisotropic transport. The ρ vs T^2 dependence measured along the direction of the nanowires indicated that the current flowed in the $LaTiO_3$ nanowires and the $SrTiO_3$ interface layers.

Acknowledgement

This work was done at the Institute for Solid State Physics of University of Tokyo from April 2005 to January 2007.

First of all and foremost, I have many people to thank for helping to make my experience enriching.

First, I would like to express my profound gratitude to Professor Mikk Lippmaa for his affectionate guidance and valuable support. I would like to express my deepest gratitude to him again for his time of checking and revising my thesis. He sometimes sends the thesis files to me via e-mail on holiday midnight.

I would like to express my great gratitude to Dr. Tsuyoshi Ohnishi for his valuable ideas, his outstanding research guidance and limitless patient. I couldn't have done anything without his help. Mr. Shinya Meguro constructed the very useful data system. Thanks to the system, data share went on smoothly. Dr. Keisuke Shibuya and Mr. Takayuki Uozumi gave me useful advices and teach me many research things. Mr. Kazunori Nishio and Mr. Yasufumi Urata helped my work and often listened to my slipslop. Mr. Sato sometimes assisted my research work. And his word often made me laugh. I hope his pretty children will grow up vigorously.

I would like to give my gratitude to Professor Takahisa Yamamoto and his students for measuring the sample by using TEM. Your excellent data is shinning in my thesis.

I would like to thank to secretaries Junko Kawamura, Rie Takahashi, Akiko Ono and Yukiko Hanada for office work and encouragement. Your work and shining smiles made my life in Kashiwa comfortable.

I'll give my acknowledgements to all my friends, who helped creating a very enjoyable and productive environment in Kashiwa.

Through it all, I owe my greatest debt to my family. Your love, patient and support are the most rewarding experience.

Achievements List

Poster presentations

- 'Characterization of LaTiO3 thin films on termination controlled SrTiO3(100) substrates'

  H. Kondo, T. Ohnishi, K. Shibuya, M. Lippmaa

  The 67th autumn meeting of the Japan Society of Applied Physics, 2006, extended abstract vol.2, p595

- 'Fabrication of conductive LaTiO3 nanowire by PLD method'

  H. Kondo, T. Ohnishi, T. Yamamoto, K. Shibuya, H. Koinuma, M. Lippmaa

  The 53th spring meeting of the Japan Society of Applied Physics, 2006, extended abstract vol.2, p640